Available online at www.sciencedirect.com
SCIENCE DIRECT®
Pergamon
Cement and Concrete Research 34 (2004) 2067–2077
CEMENT AND CONCRETE RESEARCH

Simulation model of impact on reinforced concrete

Tso-Liang Teng[a,*], Yi-An Chu[b], Fwu-An Chang[c], Hua-Sheng Chin[d]

[a]Department of Mechanical and Automation Engineering, Da-Yeh University, 112 Shan-Jiau Road, Da-Tsuen, Changhua 515, Taiwan, ROC
[b]Chung-Shan Institute of Science and Technology, P. O. Box 90008-17-10, Lung-Tan, Tao-Yuan 325, Taiwan, ROC
[c]Department of Civil Engineering, University of National Defense Chung Cheng Institute of Technology, Ta-Shi, Tao-Yuan 335, Taiwan, ROC
[d]Institute of System Engineering, University of National Defense Chung Cheng Institute of Technology, Ta-Shi, Tao-Yuan 335, Taiwan, ROC

Received 6 November 2002; accepted 9 March 2004

Abstract

This paper proposes a simple but more effective way to perform finite element analyses of impact on reinforced concrete. The equivalent inclusion method is applied and considers the reinforced concrete as a homogeneous material, simplifying the finite element meshes and greatly reducing the computational cost of analyses. Using Mori–Tanaka's average strain theory, the equivalent stiffness matrix of the homogenized material and the associated equivalent material moduli are derived for finite element analyses. The residual velocity at which a projectile penetrates into an equivalent reinforced concrete slab is studied based on the strength of the equivalent material. Two examples are presented to demonstrate the proposed method. One involves the impact of an ogive-nose projectile on a reinforced concrete slab. The FEM computational results obtained using this method are very close to the test data, implying that the proposed method will be promising in future studies of impact analyses of reinforced concrete structures. Another example of 50° oblique impact is then presented to demonstrate the dependence of projectile ricochet upon the impact velocity.

Keywords: Reinforced concrete; Impact; Finite element analyses; Equivalent inclusion method

1. Introduction

Reinforced concrete has for a long time been used to construct various defense structures, such as bunkers, shelters and command centers, among others. Consequently, the penetrability of concrete in relation to a projectile and the resistance of reinforced concrete against explosion are of high interest not only to defenders but also to developers of weapon systems. A simple but reasonable model for analyzing reinforced concrete under impacting or explosion would be a very useful tool for designers with an engineering perspective. However, the reinforcing steel bars make modeling reinforced concrete much more complex than that of plain concrete. Even when concrete is treated as a homogeneous material (matrix), the behavior of the combined material is not only inhomogeneous but also unisotropic when reinforcement is present.

Earlier studies of the penetration and perforation of plain concrete or reinforced concrete can be categorized into experimental, empirical or semiempirical, analytical and numerical simulations. Kasai et al. [1], Hanchak et al. [2], Dancygier and Yankelevsky [3] and Gomez and Shuka [4] experimentally investigated the penetration of reinforced concrete targets with steel projectiles over a range of velocity from 150 to 1000 m/s. For different material structures (e.g., concrete, soil and steel, etc.), various empirical or semiempirical formulas are available to determine the local effects of perforation, penetration, front-face spalling and back-face scabbing due to the impact of a projectile [5,6]. The Ballistic Research Laboratory (BRL), the Waterways Experiment Station (WES), the National Defense Research Committee (NDRC), and other institutions have also developed many empirical formulas from experimental data concerning the penetration of concrete [7]. McMahon et al. [8], Chang [9], Williams [10] and Yankelevsky [11] provided analytical solutions for the critical thickness of concrete panels with respect to scabbing or perforation. Forrestal and Tzou [12] developed a spherical cavity-expansion penetration model for a concrete target to predict the depth of penetration of an

* Corresponding author. Tel.: +886-4-8511221; fax: +886-4-8511224.
E-mail addresses: tlteng@mail.dyu.edu.tw, g930406@ccit.edu.tw (T.-L. Teng).

0008-8846/$ – see front matter © 2004 Elsevier Ltd. All rights reserved.
doi:10.1016/j.cemconres.2004.03.019

ogive-nose steel projectile. Sawamoto et al. [13] applied the discrete element method (DEM) to assess the local damage to reinforced concrete structures when impacted by rigid and deformable missiles at a velocity of 215 m/s. The complexity of the properties of concrete (which has randomly distributed cracks) makes developing a relatively accurate material model to predict numerically the penetration and perforation of a concrete target impacted by a projectile difficult. Consequently, Chu and Wang [14] used the finite element code LS-DYNA2D to calculate spall damage of a soil-backed concrete layer target due to projectile penetration and underground detonation. Chen [15] presented a continuum damage model to perform finite element analysis of the penetration of a concrete target to predict the residual velocity of a steel projectile with an ogive nose. Ågårdh and Laine [16] used LS-DYNA3D finite element codes to study the performance of fiber concrete against high-velocity projectiles.

This paper proposes a simpler but more effective way to perform finite element analyses of impact on reinforced concrete to estimate the depth of penetration and the residual velocity of a projectile. The equivalent inclusion method [17] is applied and reinforced concrete is considered to be a homogeneous material, simplifying the finite element meshes and greatly reducing the computational cost of the analyses. Using Mori–Tanaka's average strain theory [18], the equivalent stiffness matrix of the homogenized material model and the associated equivalent material moduli are derived for finite element analyses. Adopting Eshelby's tensor [19,20] to relate the strain field to the eigenstrains within the equivalent inclusions (the reinforcing steel bars) ensures the compatibility of the strain of the inclusions with that of the matrix, which would not otherwise be assured by the traditional rule of mixture (weighted fractions method) based on the theory of composite materials [21]. A closed form solution for Eshelby's tensor can be easily obtained by simplifying the shape of a steel bar as a cylinder of infinite length. Consequently, the numerical programming is simplified and the computation of the equivalent material moduli is greatly facilitated, making the method proposed (in this paper) very useful and practical for analyzing impacts on reinforced concrete.

An example of an ogive-nose steel projectile's impacting into a reinforced concrete slab is presented for benchmarking. A comparison with the test data [2] reveals that the proposed simulation method is very accurate and is promising for further studying the penetration of reinforced concrete structures, such as bunkers and shelters. Another example of 50° oblique impact is then presented to demonstrate the dependence of projectile ricochet upon the impact velocity.

2. Fundamental theorem

This section introduces the equivalent inclusion method [17] and applies it to consider reinforced concrete as an unisotropic homogeneous material. The reinforcing steel bars are equivalent to inclusions of the same configurations but with hypothetic internal eigenstrains. The tensor product of the eigenstrains and the associated Eshelby's tensors determines the strain fields within the inclusions. Mori–Tanaka's average stress theory [18] is then applied to investigate the overall stress–strain relations and derive the equivalent material compliance as a function of not only the material moduli of concrete and the reinforcing steel bars, but also of the volume fractions and the orientations of the equivalent inclusions.

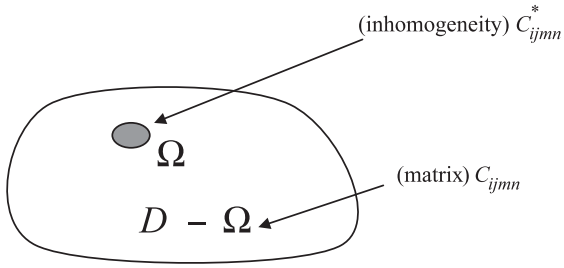

Fig. 1. Matrix and inhomogeneity.

The shapes of the steel bars are simplified to cylinders of infinite length, enabling a closed form solution involving the associated Eshelby's tensor to be obtained. The basic assumptions of the model are as follows.

1. The interfaces between the matrix and the inclusions are ideally integrated.
2. The matrix and inclusions are elastic, following the generalized Hook's law.
3. All the inclusions are regularly shaped and aligned in parallel in one or two orthogonal directions in the matrix.
4. The interactions between inclusions are negligible.

2.1. Equivalent inclusion method

Consider a finite region of a composite body D that contains an inhomogeneity with elastic moduli of C^*_{ijkl} as shown in Fig. 1. The domain of the inhomogeneity is denoted as Ω. The matrix is represented by $D-\Omega$ with elastic moduli of C_{ijkl}. Assume the finite region of composite body D is subjected to a uniform surface traction $t^\infty_j = \sigma^\infty_{ij} n_i$ where σ^∞_{ij} is the associated stress field and n_i is the outward unit normal on the boundary of D. If the inhomogeneity is absent from the domain D, then the uniform strains in D are ε^∞_{mn} and the corresponding uniform stresses are $\sigma^\infty_{ij} = C_{ijkl}\varepsilon^\infty_{kl}$. When the inhomogeneity Ω is present in D, the stress disturbances in the matrix and inclusion are denoted as σ^M_{ij} and σ^Ω_{ij}, respectively. The corresponding strain disturbances are denoted as ε^M_{mn} and ε^Ω_{ij}, respectively. Hook's law is written as,

$$\sigma^\infty_{ij} + \sigma^\Omega_{ij} = C^*_{ijmn}\{\epsilon^\infty_{mn} + \varepsilon^\Omega_{mn}\} \quad \text{in } \Omega \tag{1a}$$

$$\sigma^\infty_{ij} + \sigma^M_{ij} = C_{ijmn}\{\epsilon^\infty_{mn} + \varepsilon^M_{mn}\} \quad \text{in } D-\Omega \tag{1b}$$

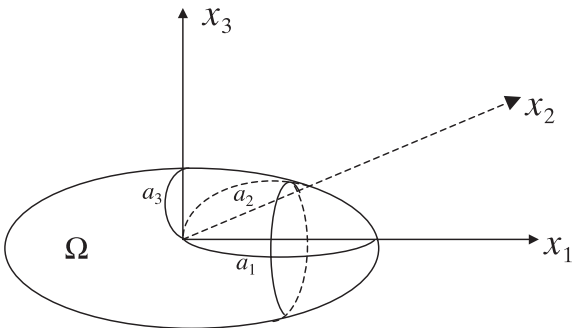

Fig. 2. An ellipsoidal inhomogeneity with principal half axes a_1, a_2 and a_3.

Let the inhomogeneity be replaced by an inclusion with the same elastic moduli C_{ijkl} as the matrix and with an equivalent eigenstrain ε^*_{mn}. Hook's law for the equivalent inclusion becomes,

$$\sigma^{\infty}_{ij} + \sigma^{\Omega}_{ij} = C_{ijmn}\{\epsilon^{\infty}_{mn} + \varepsilon^{\Omega}_{mn} - \varepsilon^*_{mn}\} \quad \text{in } \Omega \tag{2}$$

According to the equivalent inclusion method, the necessary and sufficient condition for the equivalency of the stresses and strains in the inhomogeneity and the equivalent inclusion is,

$$C^*_{ijmn}\{\epsilon^{\infty}_{mn} + \varepsilon^{\Omega}_{mn}\} = C_{ijmn}\{\epsilon^{\infty}_{mn} + \varepsilon^{\Omega}_{mn} - \varepsilon^*_{mn}\} \quad \text{in } \Omega \tag{3}$$

2.2. Strain field of the equivalent inclusion

Now, consider domain D that contains an ellipsoidal inhomogeneity Ω, defined as,

$$\Omega : \frac{x_1^2}{a_1^2} + \frac{x_2^2}{a_2^2} + \frac{x_3^2}{a_3^2} \le 1 \tag{4}$$

where a_1, a_2, and a_3 are the semiaxes of the ellipsoid, as shown in Fig. 2. Based on the equivalent inclusion method, the inhomogeneity is equivalent to an inclusion with uniform eigenstrains ε^*_{ij}. According to the Eshelby's solution [17], the associated strain disturbance due to the presence of the strain ε_{ij} within the inclusion is,

$$\varepsilon_{ij} = S_{ijmn}\varepsilon^*_{mn} \text{ in } \Omega \tag{5}$$

where S_{ijmn} is Eshelby's tensor, a function of the material moduli of the surrounding matrix C_{ijkl} and the geometry configuration of the inclusion. For the case of isotropic matrix and inclusion, Eshelby's tensor for an elliptic cylinder with $a_1 \to \infty$ and for a cylinder ($a_2 = a_3$) is written as,

$$S_{1111} = 0$$

$$S_{1122} = 0$$

$$S_{1133} = 0$$

$$S_{2222} = \frac{1}{2(1-v)}\left\{\frac{a_3^2 + 2a_2a_3}{(a_2+a_3)^2} + (1-2v)\frac{a_3}{a_2+a_3}\right\} = \frac{5-4v}{8(1-v)}$$

$$S_{3333} = \frac{1}{2(1-v)}\left\{\frac{a_2^2 + 2a_2a_3}{(a_2+a_3)^2} + (1-2v)\frac{a_2}{a_2+a_3}\right\} = \frac{5-4v}{8(1-v)}$$

$$S_{2233} = \frac{1}{2(1-v)}\left\{\frac{a_3^2}{(a_2+a_3)^2} - (1-2v)\frac{a_3}{a_2+a_3}\right\} = \frac{-1+4v}{8(1-v)}$$

$$S_{3311} = \frac{1}{2(1-v)}\left(\frac{2va_2}{a_2+a_3}\right) = \frac{v}{2(1-v)}$$

$$S_{3322} = \frac{1}{2(1-v)}\left\{\frac{a_2^2}{(a_2+a_3)^2} - (1-2v)\frac{a_2}{a_2+a_3}\right\} = \frac{-1+4v}{8(1-v)}$$

$$S_{2323} = \frac{1}{2(1-v)}\left\{\frac{a_2^2 + a_3^2}{2(a_2+a_3)^2} + \frac{1-2v}{2}\right\} = \frac{3-4v}{8(1-v)} \tag{6}$$

$$S_{3131} = \frac{a_2}{2(a_2+a_3)} = \frac{1}{4}$$

$$S_{1212} = \frac{a_3}{2(a_2+a_3)} = \frac{1}{4}$$

$$S_{2211} = \frac{1}{2(1-v)}\left(\frac{2va_3}{a_2+a_3}\right) = \frac{v}{2(1-v)}$$

where v is the Poisson's ratio of the matrix.

If domain D contains N inhomogeneities with identical configurations and the same material properties, then the averages of the stresses and the strains value over each inhomogeneities will be identical [22]. This paper proposes

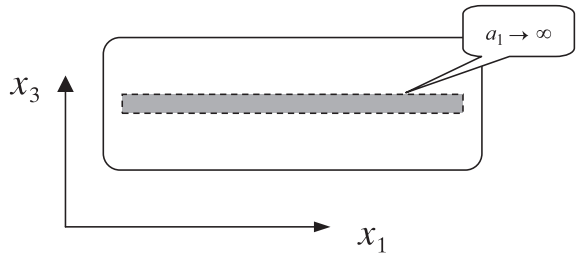

Fig. 3. One-way parallel-aligned cylindrical inhomogeneties ($a_2 = a_3$).

two arrangements of the reinforcing steel bars. The first set of one-way parallel-aligned reinforcing steel bars embedded in the concrete (matrix) will be modeled as a series of cylindrical inhomogeneities, as shown in Fig. 3. The second set of two-way orthogonal-aligned steel bars will be modeled as shown in Fig. 4. Eshelby's tensor in the perpendicular direction ($a_2 \to \infty$ and $a_1 = a_3$) can be easily obtained by cyclically permuting the subindices (1, 2 and 3) in Eq. (6).

2.3. Equivalent elastic compliance tensor

This section investigates the equivalent material compliance tensor for an isotropic elastic matrix with multiphase inclusions, based on Mori–Tanaka's average stress theory [23].

Consider a finite but sufficiently large region of composite body D, containing N distinctly shaped, randomly distributed, ellipsoidal or elliptic cylindrical inhomogeneities $\Omega = \sum_{K=1}^{N} \Omega_K$. The Kth inhomogeneity has elastic moduli $C^*_{ijkl}{}^K$ and volume fraction f_K. The surrounding matrix is denoted by $D - \Omega$ and has elastic moduli C_{ijkl}.

Assume that the body is subjected to uniform surface traction $t_j^\infty = \sigma_{ij}^\infty n_i$. When no inhomogeneities are in the domain, the uniform strain in the composite body is $\underline{\varepsilon}^\infty$ and and the corresponding uniform stress is $\underline{\sigma}^\infty = \underline{\underline{C}}\,\underline{\varepsilon}^\infty$. If the N inhomogeneities are all present in the domain, then the average stress disturbances in the matrix and the Kth inclusion are denoted as $\overline{\underline{\sigma}}^{\mathrm{M}}$ and $\overline{\underline{\sigma}}^{\Omega}_K$, respectively. The corresponding average strain disturbances are represented as $\overline{\underline{\varepsilon}}^{\mathrm{M}}$ and $\overline{\underline{\varepsilon}}^{\Omega}_K$. Consequently, the average stress can be written as,

$$\underline{\sigma}^\infty + \overline{\underline{\sigma}}^{\mathrm{M}} = \underline{\underline{C}}\left[\underline{\varepsilon}^\infty + \overline{\underline{\varepsilon}}^{\mathrm{M}}\right] \quad \text{in } D - \Omega \tag{7}$$

and the average stress in the Kth inclusion can be written as,

$$\begin{aligned}\underline{\sigma}^\infty + \overline{\underline{\sigma}}^{\Omega}_K &= \underline{\underline{C}}^*_K\left[\underline{\varepsilon}^\infty + \overline{\underline{\varepsilon}}^{\mathrm{M}} + \overline{\underline{\varepsilon}}_K\right] \\ &= \underline{\underline{C}}\left[\underline{\varepsilon}^\infty + \overline{\underline{\varepsilon}}^{\mathrm{M}} + \overline{\underline{\varepsilon}}_K - \underline{\varepsilon}^*_K\right] \quad \text{in } \Omega_K\end{aligned} \tag{8}$$

where $\overline{\underline{\varepsilon}}_K = \overline{\underline{\varepsilon}}^{\Omega}_K - \overline{\underline{\varepsilon}}^{\mathrm{M}}$ is the average strain disturbance in the Kth inclusion due to the presence of the Kth inhomogeneity itself and $\underline{\varepsilon}^*_K$ represents the hypothetic equivalent eigenstrain in the Kth inclusion. Notably, $\overline{\underline{\varepsilon}}^{\Omega}_K$ is the average strain disturbance in the Kth inclusion, due to the presence of N inhomogeneities. Because the surface traction is uniform and the inclusions are ellipsoidal, the strain disturbances $\overline{\underline{\varepsilon}}_K$ are also uniformly distributed, such that $\overline{\underline{\varepsilon}}_K = \underline{\varepsilon}_K$. According to Eshelby's solution, $\underline{\varepsilon}_K = \underline{\underline{S}}_K \underline{\varepsilon}^*_K$, where $\underline{\underline{S}}_K$ is Eshelby's tensor for the Kth inclusion due to its own presence of the inclusion.

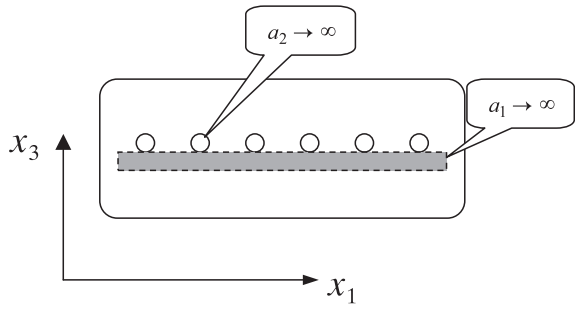

Fig. 4. Two-way orthogonal arrangement of cylindrical inhomogeneities.

Based on Mori–Tanaka's average stress theory [18], the volume average of the disturbed stresses must vanish, yielding,

$$\left[1 - \sum_{K=1}^{N} f_K\right]\overline{\underline{\sigma}}^{\mathrm{M}} + \sum_{K=1}^{N} f_K \overline{\underline{\sigma}}^{\Omega}_K = 0 \tag{9}$$

Hence, the overall strain field, $\underline{\varepsilon}$ of the composite body D can be derived as [22],

$$\underline{\varepsilon} = \underline{\varepsilon}^\infty + \sum_{K=1}^{N} f_K \underline{\varepsilon}^*_K = \overline{\underline{\underline{C}}}^{-1}\underline{\sigma} \tag{10}$$

where $\overline{\underline{\underline{C}}}^{-1}$ is the equivalent elastic compliance tensor and is written as,

$$\overline{\underline{\underline{C}}}^{-1} = \left[\underline{\underline{I}} - \sum_{K=1}^{N} f_K \underline{\underline{P}}_K^{-1}\left(\underline{\underline{C}}^*_K - \underline{\underline{C}}\right)\right]\underline{\underline{C}}^{-1} \tag{11}$$

where $\underline{\underline{P}}_K$ is defined as,

$$\underline{\underline{P}}_K = \left(\underline{\underline{C}}^*_K - \underline{\underline{C}}\right)\left[\underline{\underline{S}}_K - \sum_{K=1}^{N} f_K\left(\underline{\underline{S}}_K - I\right)\right] + \underline{\underline{C}} \tag{12}$$

and $\underline{\underline{I}}$ is the identity tensor or the so-called unit tensor.

In the case of a single-phase inclusion (i.e., $N = 1$), Eqs. (11) and (12) can be rewritten as,

$$\overline{C}^{-1}_{\mathrm{mnij}} = \left[I_{\mathrm{mnab}} - f P^{-1}_{\mathrm{mnqr}}\left(C^*_{\mathrm{qrab}} - C_{\mathrm{qrab}}\right)\right]C^{-1}_{\mathrm{abij}} \tag{13}$$

and,

$$P^{-1}_{\mathrm{ijab}} = \left\{\left(C^*_{\mathrm{ijmn}} - C_{\mathrm{ijmn}}\right)\left[(1-f)S_{\mathrm{mnab}} + f I_{\mathrm{mnab}}\right] + C_{\mathrm{ijab}}\right\}^{-1} \tag{14}$$

Similarly, based on Mori–Tanaka's average strain theory, the volume average of the disturbed strains must vanish, yielding,

$$\overline{\underline{\underline{C}}} = \underline{\underline{C}}\left[\underline{\underline{I}} + \sum_{K=1}^{N} f_K \underline{\underline{T}}_K^{-1}\left(\underline{\underline{C}}^*_K - \underline{\underline{C}}\right)\right] \tag{15}$$

where $\overline{\underline{\underline{C}}}$ is the equivalent elastic stiffness tensor and $\underline{\underline{T}}_K$ is written as,

$$\underline{\underline{T}}_K = \left(\underline{\underline{C}}^*_K - \underline{\underline{C}}\right)\underline{\underline{S}}_K - \sum_{K=1}^{N} f_K\left(\underline{\underline{C}}^*_K - \underline{\underline{C}}\right)\underline{\underline{S}}_K + \underline{\underline{C}} \tag{16}$$

2.4. Equivalent compliance tensor of reinforced concrete slabs

Embedded reinforcing steel bars in reinforced concrete slabs are typically in the two-way orthogonal arrangement, as shown in Fig. 4. Therefore, in this section, Eqs. (11) and (12) are applied to demonstrate the calculation of the equivalent elastic compliance tensor associated with the reinforced concrete slabs. From Eq. (11), the elastic compliance tensor for reinforced concrete with steel bars in a two-phase orthogonal arrangement can be shown as,

$$\overline{\underline{\underline{C}}}^{-1} = [\underline{\underline{I}} - f_1\underline{\underline{P}}_1^{-1}(\underline{\underline{C}}_1^* - \underline{\underline{C}}) - f_2\underline{\underline{P}}_2^{-1}(\underline{\underline{C}}_2^* - \underline{\underline{C}})]\underline{\underline{C}}^{-1} \quad (17)$$

where

$$\underline{\underline{P}}_1^{-1} = \{(\underline{\underline{C}}_1^* - \underline{\underline{C}})[\underline{\underline{S}}_1 - f_1(\underline{\underline{S}}_1 - I) - f_2(\underline{\underline{S}}_2 - I) + C]\}^{-1} \quad (18)$$

$$\underline{\underline{P}}_2^{-1} = \{(\underline{\underline{C}}_2^* - \underline{\underline{C}})[\underline{\underline{S}}_2 - f_1(\underline{\underline{S}}_1 - I) - f_2(\underline{\underline{S}}_2 - I) + C]\}^{-1} \quad (19)$$

Subindices 1 and 2 represent the two phases of mutually orthogonal cylindrical inhomogeneities with axes in directions of the coordinate axes x_1 and x_2, respectively.

For the two-way orthogonal arrangement of reinforcing steel bars with identical shape and material properties $\underline{\underline{C}}_1^* = \underline{\underline{C}}_2^*$; Eshelby's tensor $\underline{\underline{S}}_2$ can be obtained from $\underline{\underline{S}}_1$ in Eq. (6) by cyclically permuting the indices (1, 2 and 3). Using Voight notation, the orthotropic equivalent compliance tensor $\overline{\underline{\underline{C}}}^{-1}$ can be further transferred into a 6×6 matrix,

$$[\overline{\underline{\underline{C}}}]^{-1} = \begin{bmatrix} \frac{1}{\bar{E}_{11}} & \frac{-\bar{\nu}_{21}}{\bar{E}_{22}} & \frac{-\bar{\nu}_{31}}{\bar{E}_{33}} & 0 & 0 & 0 \\ \frac{-\bar{\nu}_{12}}{\bar{E}_{11}} & \frac{1}{\bar{E}_{22}} & \frac{-\bar{\nu}_{32}}{\bar{E}_{33}} & 0 & 0 & 0 \\ \frac{-\bar{\nu}_{13}}{\bar{E}_{11}} & \frac{-\bar{\nu}_{23}}{\bar{E}_{22}} & \frac{1}{\bar{E}_{33}} & 0 & 0 & 0 \\ 0 & 0 & 0 & \frac{1}{\bar{G}_{23}} & 0 & 0 \\ 0 & 0 & 0 & 0 & \frac{1}{\bar{G}_{31}} & 0 \\ 0 & 0 & 0 & 0 & 0 & \frac{1}{\bar{G}_{12}} \end{bmatrix} \quad (20)$$

where $\bar{E}_{ij}$, $\bar{G}_{ij}$ and $\bar{\nu}_{ij}$ are the equivalent elastic moduli, the equivalent shear moduli and the equivalent Poisson's ratio of the equivalent reinforced concrete. The value can be determined by comparing Eqs. (17) and (20).

3. Numerical verification

A numerical simulation of static bending on an RC beam based on the equivalent inclusion method had been carried out for static verification [24]. In the linear elastic range, the computational results are well compared to the test data by Bresler and Scordelies [25] and some other finite element results by directly modeling the steel bars with FE meshes and by simplifying the steel bars to be a thin steel plate [26,27]. However, the proposed method is believed to be much simple and efficient for finite element simulation.

This section considers the normal impact of 0.50 kg ogive-nose steel projectile at velocities from 300 to 1000 m/s, into a reinforced concrete slab. The numerical simulation is performed by the DYNA2D finite element codes [28] incorporated with the equivalent material moduli and compared with the test data by Hanchak et al. [2], to demonstrate the performance of the proposed model. Fig. 5 shows a 25.4-mm caliber steel projectile with a total length of 143.7 mm. The steel projectile is assumed to be elastic, perfectly plastic, with the mass density of 8000 kg/m^3, an elastic modulus of 206.9 GPa, Poisson's ratio of 0.3, yielding stress of 1.724 GPa and the CRH = 3. Fig. 6 shows the $610 \times 610 \times 178$ mm reinforced concrete. The target has three layers of square grids of reinforcing steel bars with a diameter of 5.69 mm, orthogonally arranged. The 140 MPa concrete material properties of the target, such as density, elastic moduli and Poisson's ratio are taken to be 2520 kg/m^3, 20.68 GPa and 0.18, respectively. The steel bars used here have density, elastic moduli and Poisson's ratio of 7850 kg/m^3, 199 GPa and 0.3, respectively.

The following subsections describe the calculation of the equivalent material moduli of the reinforced concrete target, using the equivalent inclusion method. The finite element model and the numerical results are then presented.

3.1. Effective material moduli of the target

This subsection determines the equivalent material moduli using the equivalent inclusion method described in Section 2.

First, Eshelby's tensors $\underline{\underline{S}}_1$ and $\underline{\underline{S}}_2$ of the reinforced concrete slab are calculated by directly substituting Poisson's ratio of the matrix (the original concrete) into Eq. (6). Table 1 lists the data associated with $\underline{\underline{S}}_1$ and $\underline{\underline{S}}_2$. Substituting the values of $\underline{\underline{S}}_1$ and $\underline{\underline{S}}_2$ and the associated volume fractions $f_1 = f_2 = 0.005$ into Eqs. (17), (18) and (19) yields the

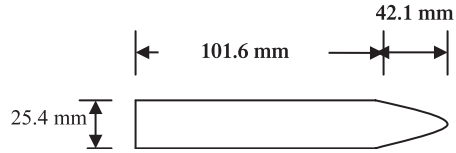

Fig. 5. Steel penetrator geometry [2].

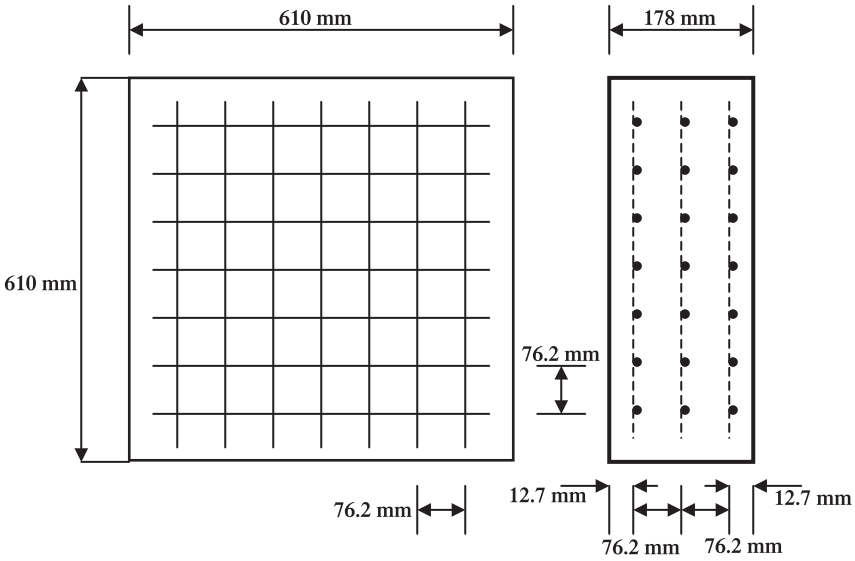

Fig. 6. Reinforced concrete target geometry [2].

equivalent compliance tensor $\overline{\underline{\underline{C}}}^{-1}$. Finally, the associated equivalent elastic moduli $\bar{E}_{ij}$, shear moduli $\bar{G}_{ij}$ and Poisson's ratio $\bar{v}_{ij}$ of the reinforced concrete material are determined from Eq. (20), and presented in Table 2. The properties of the equivalent material are orthotropic because the reinforcing steel bars are aligned orthogonally in the concrete slab. Because the volume fractions are equal, $f_1 = f_2$, the components of the material moduli in directions x_1 and x_2 are equal.

3.2. Finite element model

Fig. 7 shows the finite element model of the normal impact of an ogive-nose steel projectile, at velocities from 300 to 1000 m/s, into a reinforced concrete slab. For reasons of symmetry, only one half of the cross-section is modeled with 5177 quadrilateral elements and 5363 nodes, to approximate the target under a plane strain assumption. Constraint of nodal displacement in x_1 direction is applied on the plane of symmetry ($x_1 = 0$). Another constraint of nodal displacement in x_3 direction is applied on the right lower corner of the slab. An erosion algorithm is used to alleviate the excessive element distortion problem and to model the fracturing phenomena of the reinforced concrete target. Two erosion criteria, shear failure and tensile cut-off, are implemented into the finite element code as,

$$\bar{\varepsilon}' = \sqrt{\frac{2}{3}\varepsilon'_{ij}\,\varepsilon'_{ij}} \geq f_s \tag{21}$$

$$\varepsilon_{kk} \geq f_t \tag{22}$$

where $\varepsilon'_{ij} = \varepsilon_{ij} - \varepsilon_{kk}/3$ are the deviatoric strains; $\bar{\varepsilon}'$ is defined as the effective shear strain, ε_{kk} is the volumetric strain, f_s and f_t are the shear erosion strain and the tensile erosion strain, respectively. When one of the two erosion conditions is reached, the erosion algorithm removes the associated element. Erosion strains f_s and f_t are both just hypothetical values for numerical simulation, and are not determined from field experimental data. In general, the erosion algorithm is introduced into the Lagrangian finite element codes for carrying out penetration calculations. However, the associated erosion strain may not be identical to the fracture strain. According to the author of the DYNA2D codes [29], a computational erosion strain (strain required for an element to be deleted) has to be defined to use the erosion algorithm. The erosion strain

Table 1
Eshelby's tensor

$a_1 \to \infty, (a_2 = a_3)$		$a_2 \to \infty, (a_1 = a_3)$	
Matrix Poisson's ratio	0.18	Matrix Poisson's ratio	0.18
$S_{1111} = S_{1122} = S_{1133}$	0	$S_{2211} = S_{2222} = S_{2233}$	0
$S_{2211} = S_{3311}$	0.1097	$S_{1122} = S_{3322}$	0.1097
$S_{2233} = S_{3322}$	−0.0426	$S_{1133} = S_{3311}$	−0.0426
$S_{2222} = S_{3333}$	0.6524	$S_{1111} = S_{3333}$	0.6524
S_{2323}	0.3475	S_{3131}	0.3475
$S_{3131} = S_{2121}$	0.25	$S_{2323} = S_{1212}$	0.25

Table 2
Equivalent material properties

Material properties	Unreinforced concrete	Reinforced concrete
Density (kg/m^3)	2520	2565
Principal elastic modulus $\bar{E}_{11}$ (GPa)	20.68	20.8
Principal elastic modulus $\bar{E}_{22}$ (GPa)	20.68	20.8
Principal elastic modulus $\bar{E}_{33}$ (GPa)	20.68	20.7
Poisson's ratio $\bar{v}_{12}$	0.18	0.175
Poisson's ratio $\bar{v}_{13}$	0.18	0.175
Poisson's ratio $\bar{v}_{23}$	0.18	0.172
Shear modulus $\bar{G}_{12}$ (GPa)	8.7	9

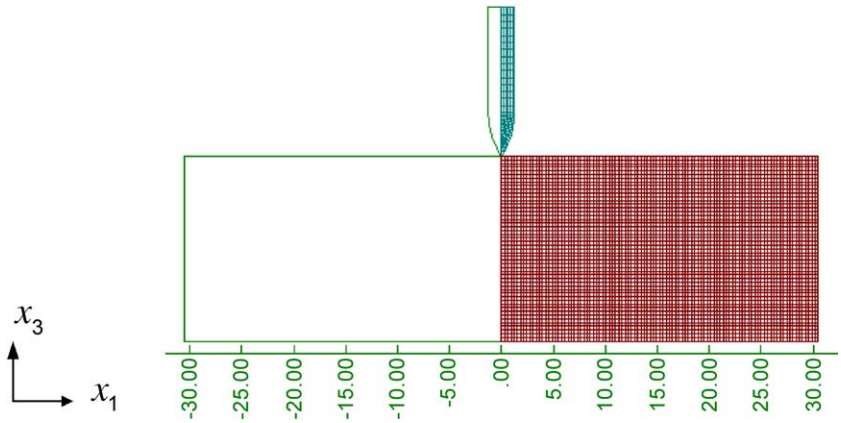

Fig. 7. Finite element model for perforation calculations.

determines when an element is thought to no longer contribute to the penetration process. It must therefore be somewhat dependent upon the material properties. However, it is difficult to relate this erosion strain to any single measurable parameter. For example, the erosion strain is not identical to the fracture strain. In a low-ductility material, the material could fracture before it erodes. In this paper, the erosion strains f_s and f_t, are first determined by matching the numerically calculated residual velocity with the measured data for a few, typically one or two, specific impact velocities. Then, the same criteria are applied to calculate numerically other impact velocities.

In this paper, another function of the erosion criteria is to compensate the inability of the equivalent inclusion method for handling the failure behavior of materials. Therefore, the equivalent material is assumed to be linear–elastic up to failure, which is expected to be viable for modeling the tensile and shear fractures of the concrete slab under impact loadings.

3.3. Numerical results concerning normal impact phenomena

When a massive reinforced concrete slab suffers a direct hit, the forces generated at impact and during the penetration process can easily break up large masses of reinforced concrete, unless sufficient reinforcing steel is present to inhibit the spread of the cracks. Therefore, reinforcement tends to counteract the brittleness of the concrete and provide tensile strength.

In the numerical calculation, both of the erosion strains f_s and f_t are set to 0.075, which are determined by matching the numerically calculated residual velocity with the measured data for impact velocities of 587 and 743 m/s. Fig. 8a and b display the deformed mesh plots of different stages of the penetration of a steel projectile into a reinforced concrete slab at 382 m/s. The penetration process of the projectile can be simulated by two simple stages. In the first (Fig. 8a), at up to 300 μs, the projectiles partially penetrate into the target and cause damage near the rear face of the slab. At this time, the curved shear cracks and bell-shaped scabbing had been already caused by the shock waves and associated rarefaction waves. It is estimated that the cracks are first initiated at about 60 μs, which is slightly later than the first shock front reflected from the rear surface. In this case, the front crater is not as real as the general experimental results, because the erosion algorithm removes the crushed elements.

In the second stage (Fig. 8b), at up to 1050 μs, the projectile pushes the scabbing part, shears it off the surrounding material and continues penetrating the slab. The thickness of the perforation of the target is that required to penetrate and completely shear off the scabbing part, completely stopping the projectile and the scabbing.

When the reinforced concrete slab is perforated, the velocity of the projectile remains constant because the slab material can no longer offer any resistance. This constant velocity is defined as the residual velocity of the projectile. If perforation does not occur, the projectile rests in the slab with zero residual velocity.

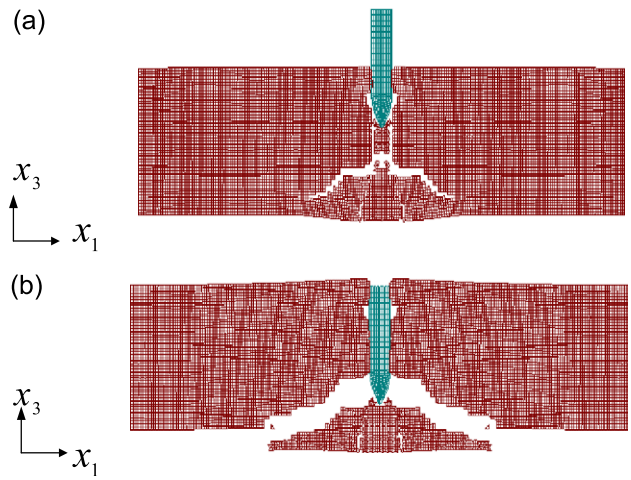

Fig. 8. (a) Normal penetration, Stage I (impact velocity of 382 m/s, $t = 300$ μs). (b) Normal penetration, Stage II (impact velocity of 382 m/s, $t = 1050$ μs).

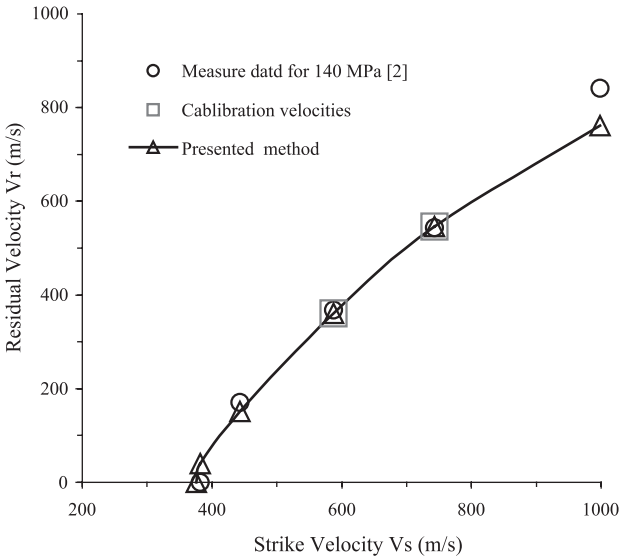

Fig. 9. Comparison of FEA numerical results and test data of Hanchak et al. [2].

A series of calculations were performed to predict the residual velocities of an ogive-nose steel projectile that impacts a reinforced concrete slab at velocities from 300 to 1000 m/s. Fig. 9 compares the numerical results with the test data of Hanchak et al. [2]. The residual velocities, predicted by the proposed finite element simulation to vary with the impact velocities, agree with the test data. In Fig. 9, the ballistic limit predicted by the proposed finite element calculation is 376 m/s, which is about 1.6% lower than the test data of 382 m/s.

Some of the axi-symmetric behavior in this problem may not be considered well enough. An advanced analysis will be conducted by 3D finite element codes in the future.

4. Oblique impact effect

This section considers an oblique impact of the same ogive-nose projectile into the same reinforced concrete slab. The angle between the projectile's trajectory and the normal to the target slab is called the angle of obliquity, which is shown in Fig. 10. The numerical techniques used to simulate an oblique impact on the slab are the same as those used to simulate of normal impact.

4.1. Projectile and target modeling

Plane strain analysis is performed using the DYNA2D finite element model and the geometry is fully considered to simulate an oblique impact at 50°. The model comprises 10,354 quadrilateral elements and 10,643 nodes, as shown in Fig. 11. Constraints of nodal displacements in horizontal and vertical directions are applied on the left and right (vertical) sides of the target meshes. The equivalent material properties are presented in Table 2 and the

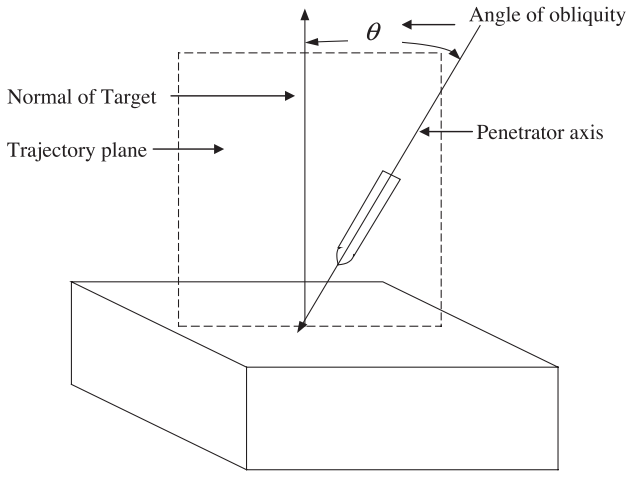

Fig. 10. Illustration of impact nomenclature.

erosion strains are the same as in the case of normal impact. The method of modeling the oblique impact is identical to that used to model the normal impact except for the arrangement of the finite element meshes and the boundary conditions. In oblique impact, tunneling by a penetrating projectile follows from the substantial erosion of the target material elements. The striking velocity primarily determines the physical mechanisms that operate when the slab is impacted. Here, a 50° oblique impact of the projectile into a 178-mm thick target slab at two velocities, 600 and 1000 m/s, is considered. The impact velocities are selected because they can elucidate the

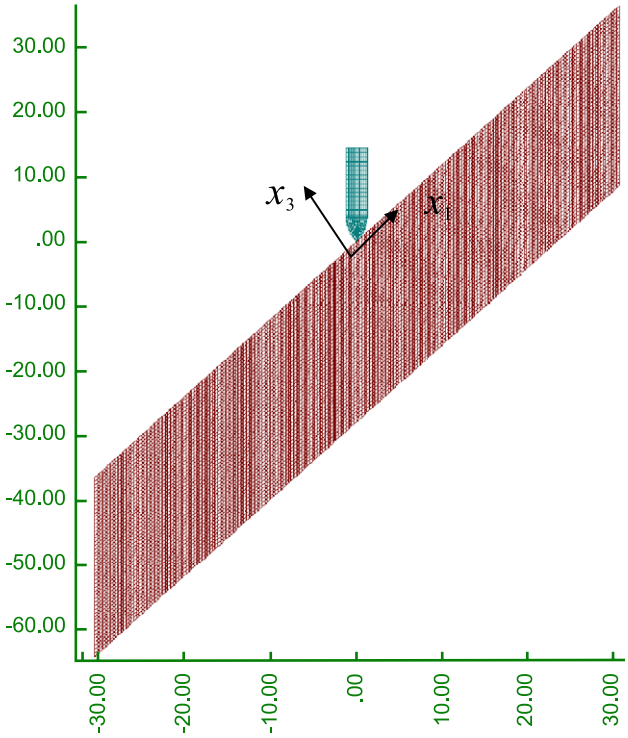

Fig. 11. Finite element model for 50° oblique impact of reinforced concrete slab.

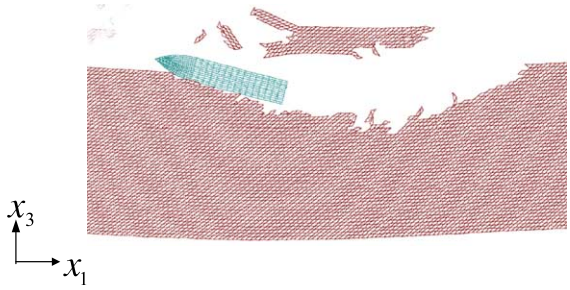

Fig. 12. Fifty degrees oblique impact for reinforced concrete slab, Vs = 600 m/s, at 900 μs.

characteristics of interesting failure phenomena associated with the penetration and the perforation of the reinforced concrete slab.

4.2. Computational results

Fig. 12 presents the results of the oblique impact at 600 m/s after 900 μs. The tangential velocity component of the projectile is larger than the normal velocity component; therefore, the nose tip of the projectile makes a shallow crater (to a depth of about 1/3 the thickness of the slab) at the front surface of the target. The projectile is finally deflected outward (rebound) from the target, causing it to rotate clockwise. The timing and effect of this final clockwise rotation depend on the magnitude of the two translation velocities (normal and tangential to the slab's surface), the combined rotational velocity and the depth of penetration of the projectile.

The same example, but for unreinforced concrete slab, is present in Fig. 13 for reference. The projectile is embedded into the unreinforced concrete slab, because the stiffness of the unreinforced concrete slab is not as strong as the one with reinforcing steel bars (cf. Table 2).

At higher impact velocities, the projectile creates a hole and successively perforates the reinforced concrete slab. The instantaneous radius of the tunnel depends on the shape of the projectile's nose tip and the two components of translation velocity. Fig. 14(a)–(d) plot the deformed meshes after four specific intervals during the perforation by the steel projectile of the target slab at 1000 m/s. Fig. 14 reveals that the steel projectile initially obliquely penetrates the target

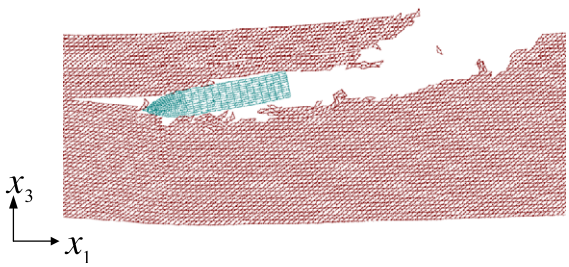

Fig. 13. Fifty degrees oblique impact for unreinforced concrete slab, Vs = 600 m/s, at 900 μs.

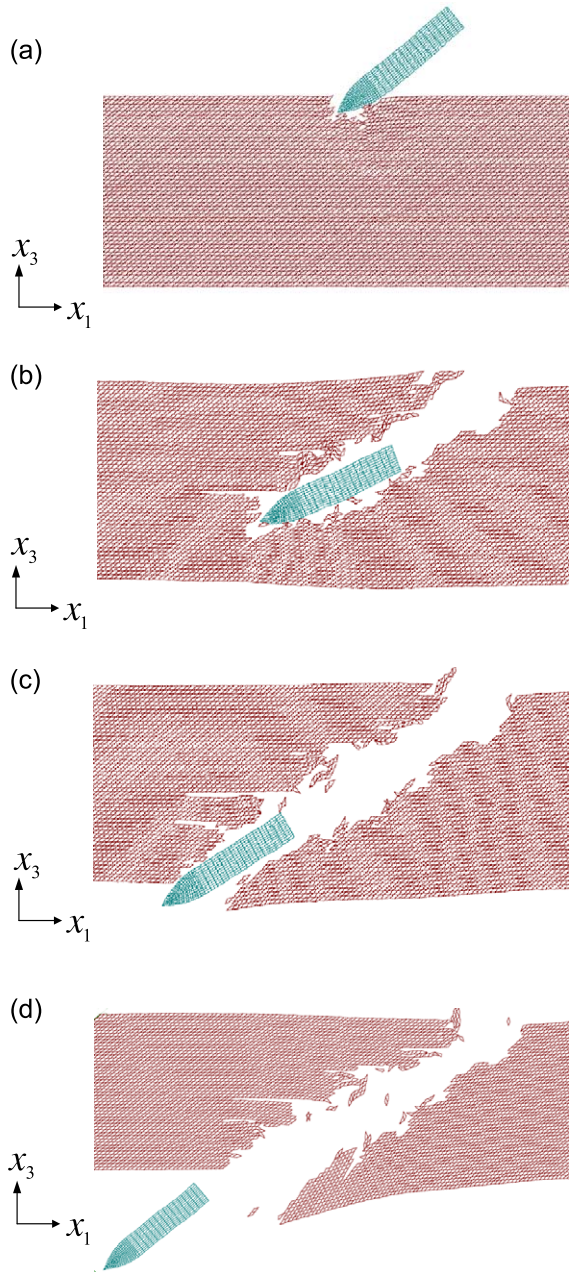

Fig. 14. (a) Fifty degrees oblique impact for reinforced concrete slab, Vs = 1000 m/s, at t = 30 μs. (b) Fifty degrees oblique impact for reinforced concrete slab, Vs = 1000 m/s, at t = 300 μs. (c) Fifty degrees oblique impact for reinforced concrete slab, Vs = 1000 m/s, at t = 480 μs. (d) Fifty degrees oblique impact for reinforced concrete slab, Vs = 1000 m/s, at t = 700 μs.

and then follows a slight downward bent curve trajectory until it finally perforates the slab at approximately 700 μs. The formation of the path of penetration and of the exit craters clearly produce intense shock waves upon impact. The waves propagated into both the target slab and the projectile, causing the right side of the exit crater to bend outward.

The empirical results of similar tests are not obtained by the authors. The authors conduct a series of numerical analyses on the ricochet limits of the similar projectile

against a reinforced concrete target based on the proposed method. The computational results are compatible with the Tate's semiempirical formula (1979) for the ricochet limit as a function of the impact velocity qualitatively [30].

5. Conclusions

This paper applied the equivalent inclusion method to reinforced concrete slabs as homogeneous orthotropic materials, to evaluate the equivalent material strength of such slabs in subsequent finite element analyses. The residual velocity of a projectile that penetrates into an equivalent reinforced concrete slab is considered based on the equivalent material strength.

The normal impact of an ogive-nose steel projectile, at velocities from 300 to 1000 m/s, into a reinforced concrete slab is examined. The numerical results and the test data are compared. The variation of the residual velocities with the impact velocities, as predicted by the proposed finite element simulation, agrees with the test data. The penetration at a low-impact velocity of 382 m/s is displayed. Given the shear and tensile cut-off failure criteria, the formation of a bell-shaped scabbing is predicted, based on the proposed finite element simulation.

Oblique impact at 50° is then considered. At a low-impact velocity of 600 m/s, the projectile is embedded into the unreinforced concrete slab, but it can only penetrate one third of the way through the reinforced concrete slab and is then deflected (ricocheted) from the slab. At a higher impact velocity of 1000 m/s, the projectile can perforate the reinforced concrete target slab, implying that increasing the impact velocity increases the ricochet angle of penetration. No attempt was made here to estimate the ricochet angle associated with various impact velocities and different materials. Such research will be performed in further studies.

A simple but reasonably effective model of penetration of reinforced concrete structures is very useful and valuable, especially for designers of military defense structures, weapon systems, nuclear power plants, and other facilities. The proposed model, based on the equivalent inclusion method proposed in this paper, provides an alternative way to study the penetrability of reinforced concrete slabs. The method is very efficient for finite element analyses. Numerical results demonstrate the viability of the proposed model of the impact on reinforced concrete.

Appendix A.

Notation list

a_1, a_2, a_3 Semiaxes of the ellipsoidal inhomogeneity
C_{ijkl} or $\underline{\underline{C}}$ Elastic moduli of matrix
C^*_{ijkl} Elastic moduli of inhomogeneity
$C^{*\,k}_{ijkl}$ or $\underline{\underline{C}}^*_K$ Elastic moduli of the Kth inhomogeneity
$\overline{\underline{\underline{C}}}$ Equivalent elastic stiffness tensor
$\overline{\underline{\underline{C}}}^{-1}$ Equivalent elastic compliance tensor
$\overline{E}_{ij}$ Equivalent elastic moduli
f_K Volume fraction of the Kth inhomogeneity
f_s Shear erosion strain
f_t Tensile erosion strain
$\bar{G}_{ij}$ Equivalent shear moduli
$\underline{\underline{I}}$ Unit tensor
n_i Outward unit normal
S_{ijmn} Eshelby's tensor
$\underline{\underline{S}}_K$ Eshelby's tensor for the Kth inclusion
t_j^∞ A uniform surface traction

Greek letters

Ω Domain of inhomogeneity
ν Poisson's ratio
$\bar{\nu}_{ij}$ The equivalent Poisson's ratio
σ^∞_{ij} or $\underline{\sigma}^\infty$ Stress field due to the uniform surface traction
σ^M_{ij} Stress disturbance in matrix
$\overline{\underline{\sigma}}^M$ Average stress disturbance in matrix
σ^Ω_{ij} Stress disturbance in inclusion
$\overline{\underline{\sigma}}^\Omega_K$ Average stress disturbance in the Kth inclusion
ε^∞_{mn} or $\underline{\varepsilon}^\infty$ Uniform strain in the composite body
ε^M_{mn} Strain disturbance in matrix
ε^Ω_{ij} Strain disturbance in inhomogeneity
$\overline{\underline{\varepsilon}}^M$ Average strain disturbance in the matrix
$\overline{\underline{\varepsilon}}^\Omega_K$ Average strain disturbance in the Kth inhomogeneity
$\underline{\varepsilon}_K$ Uniform strain disturbance in the Kth inclusion
$\overline{\underline{\varepsilon}}_K$ Average strain disturbance in the Kth inclusion
ε^*_{mn} Equivalent eigenstrain
$\underline{\varepsilon}^*_K$ Hypothetic equivalent eigenstrain in the Kth inclusion
ε'_{ij} Deviator strain
$\bar{\varepsilon}'$ Effective shear strain
ε_{kk} Volumetric strain

References

[1] Y. Kasai, H. Tsubota, T. Ohno, K. Kogure, T. Uchida, Experimental study on impact resistance of reinforced concrete slabs with thin steel plates against projectile impact, Proc Int Symp Impact Eng 1 (1992) 211–216.
[2] S.J. Hanchak, M.J. Forrestal, E.R. Young, J.Q. Ehrgott, Perforation of concrete slabs with 48 MPa (7 ksi) and 140 MPa (20 ksi) unconfined compressive strengths, Int J Impact Eng 12 (1) (1992) 1–7.
[3] A.N. Dancygier, D.Z. Yankelevsky, High strength concrete response to hard projectile impact, Int J Impact Eng 18 (6) (1996) 583–599.
[4] J.T. Gomez, A. Shuka, Multiple impact penetration of semi-infinite concrete, Int J Impact Eng 25 (2001) 965–979.
[5] A.K. Kar, Projectile penetration into buried structures, J Struct Div., Proc.-Am Soc Civ Eng 104 (ST1) (1978) 125–139.
[6] A. Haldar, H.A. Hamieh, Local effect of solid missiles on concrete structures, J Struct Eng 110 (5) (1984) 948–960.
[7] H. Adeli, A.M. Amin, Local effect of impactors on concrete structures, Nucl Eng Des 88 (1985) 301–317.
[8] P. McMahon, B.L. Meyers, K.P. Buchert, Impact of deformable missiles on concrete walls, J Power Div., Proc.-Am Soc Civ Eng 104 (PO1) (1978) 183–197.
[9] W.S. Chang, Impact of solid missiles on concrete barriers, J Struct Div., Proc.-Am Soc Civ Eng 107 (ST2) (1981) 257–271.
[10] M.S. Williams, Modeling of local impact effects on plain and reinforced concrete, ACI Struct J 91 (2) (1994) 179–187.

[11] D.Z. Yankelevsky, Local response of concrete slabs to low velocity missile impact, Int J Impact Eng 19 (4) (1997) 331–343.
[12] M.J. Forrestal, D.Y. Tzou, A spherical cavity-expansion model for concrete targets, Int J Solids Struct 34 (31–32) (1997) 4127–4146.
[13] Y. Sawamoto, H. Tsubota, Y. Kasai, N. Koshika, H. Morikawa, Analytical studies on local damage to reinforced concrete structures under impact loading by discrete element method, Nucl Eng Des 179 (1998) 157–177.
[14] Y.A. Chu, J.P. Wang, A numerical study on penetration and underground detonation damage of concrete target, The 13th International Symposium on Ballistics Stockholm, Sweden, (1–3) June (1992).
[15] E.P. Chen, Numerical implementation of a brittle damage model and its application to concrete slab perforation, PVP-Vol. 343, Validation, Development, and Application of Inelastic Methods for Structural Analysis and Design ASME (1996) 147–152.
[16] L. Ågårdh, L. Laine, 3D FE-simulation of high velocity fragment perforation of reinforced concrete slabs, Int J Impact Eng 22 (4) (1999) 911–922.
[17] T. Mura, Micromechanics of Defects in Solids, 2nd, revised edition, Kluwer Academic Publishing, Netherlands, 1987.
[18] T. Mori, K. Tanaka, Average stress in matrix and average elastic energy of materials with misfitting inclusion, ACTA Metall 21 (1973) 571–574.
[19] J.D. Eshelby, The determination of the elastic field of an ellipsoidal inclusion, and related problems, Proc R Soc Lond A241 (1957) 376–396.
[20] J.D. Eshelby, The elastic field outside an ellipsoidal inclusion, Proc R Soc Lond A252 (1959) 561–569.
[21] B.D. Agarwal, L.J. Broutman, Analysis and Performance of Fiber Composites, second edition, Wiley, New York, 1990.
[22] L.P. Chao, J.H. Hung, Prediction of elastic moduli of porous materials with equivalent inclusion method, J Reinf Plast Compos 18 (7) (1999) 592–605.
[23] J.H. Hung, Effective electroelastic moduli of multiphase piezoelectric composites, J Chin Soc Mech Eng 17 (2) (1996) 111–121.
[24] T.L. Teng, Y.A. Chu, H.S. Chin, The application of equivalent inclusion method in reinforced concrete structure analyses, Chin J Mech., Ser B 19 (1) (2003) 17–28.
[25] B. Bresler, A.C. Scordelies, Shear strength of reinforced concrete beam—Series II, SESM Report, No. 64-2, University of California, Berkeley, December, 1964.
[26] M. Suidan, W.C. Schnobrich, Finite element analysis of reinforced concrete, J Struct Div., ASCE 99 (ST. 10) (1973) 2109–2122.
[27] C.S Lin, A.C. Scordelis, Nonlinear analysis of reinforced concrete shells of general form, J Struct Div., ASCE 101 (ST. 3) (1975) 523–538.
[28] J.O. Hallquist, LS-DYNA2D—An Explicit two dimensional hydrodynamic finite element code with interactive rezoning and graphical display. Technical Report LSTC Report 1004, Livermore Software Technology Corporation, Livermore, California, 1990.
[29] D.A. Sewell, A.C.J. Ong, J.O. Hallquist, Penetration calculation using an erosion algorithm in DYNA, Proceedings of the 12th International Symposium on Ballistics, San Antonio 3 (1992) 208–217.
[30] T.L. Teng, Y.A. Chu, F.A. Chang, H.S. Chin, Numerical Analysis of Oblique Impact on Reinforced Concrete, Cem Concr Compos (2004).